The 1985 Biomass Burning Season in South America: Satellite Remote Sensing of Fires, Smoke, and Regional Radiative Energy Budgets

SUNDAR A. CHRISTOPHER, MIN WANG, TODD A. BERENDES, AND RONALD M. WELCH

Department of Atmospheric Sciences, Global Hydrology and Climate Center, University of Alabama in Huntsville, Huntsville, Alabama

SHI-KENG YANG

Climate Prediction Center/NCEP, Washington, D.C.

(Manuscript received 3 March 1997, in final form 3 November 1997)

ABSTRACT

Using satellite imagery, more than five million square kilometers of the forest and cerrado regions over South America are extensively studied to monitor fires and smoke during the 1985 biomass burning season. The results are characterized for four major ecosystems, namely, 1) tropical rain forest, 2) tropical broadleaf seasonal, 3) savanna/grass and seasonal woods (SGW), and 4) mild/warm/hot grass/shrub (MGS). The spatial and temporal distribution of fires are examined from two different methods using the multispectral Advanced Very High Resolution Radiometer Local Area Coverage data. Using collocated measurements from the instantaneous scanner Earth Radiation Budget Experiment data, the direct regional radiative forcing of biomass burning aerosols is computed. The results show that more than 70% of the fires occur in the MGS and SGW ecosystems due to agricultural practices. The smoke generated from biomass burning has negative instantaneous net radiative forcing values for all four major ecosystems within South America. The smoke found directly over the fires has mean net radiative forcing values ranging from -25.6 to -33.9 W m^{-2}. These results confirm that the regional net radiative impact of biomass burning is one of *cooling.* The spectral and broadband properties for clear-sky and smoke regions are also presented that could be used as input and/or validation for other studies attempting to model the impact of aerosols on the earth–atmosphere system.

These results have important applications for future instruments from the Earth Observing System (EOS) program. Specifically, the combination of the Visible Infrared Scanner and Clouds and the Earth's Radiant Energy System (CERES) instruments from the Tropical Rainfall Measuring Mission and the combination of Moderate Resolution Imaging Spectrometer and CERES instruments from the EOS morning crossing mission could provide reliable estimates of the direct radiative forcing of aerosols on a global scale, thereby reducing the uncertainties in current global aerosol radiative forcing values.

1. Introduction

Each year in the Tropics, extensive areas of the forests and savannas are burned for agricultural purposes and to accommodate the needs of the expanding population (Andreae 1991). The permanent deforestation is replaced with grazing or crop land, while the land cleared for agricultural purposes is primarily used for shifting agriculture. Although burning takes place whenever there is plant material that is dry, biomass burning is concentrated between July and October (e.g., Setzer and Perreira 1991) in the Southern Hemisphere and between December and April (e.g., Cahoon et al., 1992a) in the Northern Hemisphere. Estimates from Lanly (1982) show that tropical forests cover 1440 million ha, while the savannas cover approximately 1530 ha. The most commonly used values of tropical deforestation from the Food and Agriculture Organization (1988) are around 75 000 km^2 yr^{-1} by the late 1970s and expected to be higher for the 1980s and beyond (Myers 1991). Similar estimates are reported by Meillo et al. (1985) and Molofsky et al. (1986). Shifting agriculture, on the other hand, covers 300–500 million ha (Seiler and Crutzen 1980) and is not expected to rise (Andreae 1991) because virgin land used for such purposes is becoming increasingly scarce. Instead, this land is now used for permanent agriculture, which, due to continued use, could become unsuitable for these purposes. In recent years, the effect of biomass burning on a global and regional scale has received due attention because of its effect on atmospheric chemistry (Fishman, 1991; Hao and Liu 1994; Reichle et al. 1986), radiation budget (Penner et al. 1992; Coakley et al. 1983; Christopher et al. 1996), increasing greenhouse gases (Ward et al.

Corresponding author address: Dr. Sundar A. Christopher, Department of Atmospheric Sciences, University of Alabama in Huntsville, 977 Explorer Blvd., Huntsville, AL 35899.
E-mail: sundar@atmos.uah.edu

1992), loss of biodiversity (Uhl et al. 1988), decreasing evapotranspiration and rainfall from altered general circulation patterns (Nobre et al. 1991), increasing surface albedo and runoff (Gentry and Lopez-Parodi 1980), and spread of plant and human diseases via colonization (Kingman 1989). The wide variety of satellite data from current and future instruments can be used to address these issues.

Satellite measurements have been used to routinely measure various aspects of biomass burning. Much attention has been focused upon detecting fires from biomass burning on a regional scale (Flannigan and Vonder Haar 1986; Matson and Stephens 1987; Tucker et al. 1984; Malingreau et al. 1985; Setzer and Perreira 1991; Kaufman et al. 1990; Lee and Tag 1990; Justice et al. 1996). These studies have examined fires over South America, Africa, and Southeast Asia. The commonly used Advanced Very High Resolution Radiometer (AVHRR) dataset is either in the high-resolution picture transmission or local area coverage (LAC) (Kidwell 1995) format at a nominal spatial resolution of 1 km, while the global area coverage data at a nadir ground spatial resolution of 4 km have been tested in selected studies (Belward et al. 1994; Malingreau et al. 1985). Although the AVHRR data has been used to obtain fire counts, several challenges continue to exist. For example, the infrared channels that are used to detect these fires often saturate well below the temperature of the fires, thereby making exact fire counts difficult. Other difficulties include spatial sampling and the time of satellite overpass that may not coincide with peak fire activities. An extensive review of the various fire detection schemes is presented in Kennedy (1992) and Justice and Dowty (1994). Robinson (1991) reviews the limitations in using AVHRR imagery for fire detection. While the AVHRR has remained the workhorse for fire detection, recent studies have utilized the geostationary satellites (Prins and Menzel 1992, 1994; Weaver et al. 1995) to monitor fires. A distinct advantage is the improved temporal frequency because GOES imagery is typically available every hour. In fact, the AVHRR time of overpass is at least 2 h after the peak burning activity (Prins and Menzel 1994). However, small-scale fires that are detectable by AVHRR could be missed in GOES imagery due to the coarser spatial resolution of the GOES imagers and sounders, although the GOES instruments typically saturate at a higher temperature than the AVHRR. Until the launch of the Moderate Resolution Imaging Spectrometer (MODIS) instrument on the Earth Observing System Morning Crossing platform, the AVHRR will remain the preferred instrument for obtaining fire counts on a regional basis. Recent international collaborations have also provided the research community with a global 1-km AVHRR dataset (Eidenshink and Faundeen 1994) that could be used for mapping fires on a global basis, although data volumes are difficult to handle. Reliable estimates of global fire counts could be used as input to trace gas transport models, regional emission models, and mesoscale models of atmospheric chemistry (Kaufman and Justice 1994). Furthermore, burned-area estimates (Cahoon et al. 1992b) derived from fire counts could be used to drive regional-scale ecological process models (Frohn et al. 1996). Fire distribution and frequency, along with ground-based information on particulate concentrations, can also be used to derive estimates of trace gas concentrations from satellite data (Kaufman et al. 1990).

While the detection of fires from AVHRR imagery is performed on a routine basis, an automated ''smoke'' detection scheme is still lacking. Much of the difficulty is due to the bright backgrounds over which smoke from biomass burning is generated. Other concerns are the limited number of spectral channels available from the AVHRR and, therefore, the difficulty in separating clouds and smoke from spectral information alone. Most studies provide only a qualitative view of the smoke, and there is no comprehensive information on the spatial information of smoke on a quantitative basis. The most common technique to separate smoke and clouds and the underlying background is to use a simple set of thresholds (Kaufman et al. 1990). Other techniques include the dark-surface approach (Fraser et al. 1984; Kaufman and Sendra 1988) and regions where sharp contrast is available (Tanre et al. 1988). While dense smoke can be distinguished from the underlying background, in this method, it is difficult to properly identify the optically thin hazelike smoke. Another method uses the textural (spatial) information from satellite imagery to separate the dense smoke, haze, and clouds from the underlying background (Christopher et al. 1996). This technique has been tested on a limited set of images over South America and is yet to be fully automated. A global smoke product could be used in studies that 1) calculate the radiative forcing of aerosols from biomass burning (Anderson et al. 1996; Christopher et al. 1996; Christopher and Chou 1997), 2) estimate surface fluxes below aerosol layers (Konzelmann et al. 1996), and 3) estimate, on a routine basis, the distribution of smoke between land and ocean. This information can be used as validation and/or input to the general circulation models (GCMs). This product could also include aerosols from nonfire related events such as dust storms.

Although it has been well established that aerosols play a significant role on the radiation balance of the earth–atmosphere system, no comprehensive picture has yet emerged on how to obtain the radiative effects of aerosols on a global scale. The radiative effects of aerosols are often classified into two categories, namely, the ''direct effect'' (Penner et al. 1992; Anderson et al. 1996), where the atmospheric aerosols scatter the incoming solar radiation, thereby increasing the amount of solar radiation reflected to space causing a ''cooling effect,'' and the ''indirect effect'' (Schwartz 1988; Kaufman and Fraser 1997), where the aerosols act as cloud condensation nuclei and modify the shortwave reflective

properties of clouds. This effect could cause either ''cooling'' or ''warming'' depending upon the optical properties of clouds. Kaufman (1995) provides an extensive review of the indirect and direct effects of aerosol radiative forcing. Current estimates of the global direct effect of biomass burning range from -0.8 (Penner et al. 1992) to -0.2 W m^{-2} (Hobbs et al. 1997). Chylek and Wong (1995) also show that the direct radiative forcing of smoke aerosols is a sensitive function of the size distribution of aerosol particles. Their results show that the direct radiative forcing varies from -0.2 to -1.1 W m^{-2} for the range of measured size distributions. These studies use a simple radiative transfer equation that is valid only for aerosols with optical depths less than 0.2. These equations involve several assumptions that include values for 1) rate of biomass burning; 2) lifetime of smoke; 3) fraction of burned material that goes into smoke; 4) surface albedo; 5) fractional cloud cover; 6) optical properties of aerosols that include single scattering albedo, optical depth, and extinction coefficients; and 7) fraction of smoke that is distributed between land and ocean. The rate of biomass burning is compiled from statistics valid for the period 1975–80 (Crutzen and Andreae 1990); the lifetime of smoke is assumed to be 6 days (Charlson et al. 1992), which is valid for sulfate aerosols; the surface albedo is assumed to be 15%; and the global cloud cover is assumed to be 61%. These assumptions were used by both Penner et al. (1992) and Hobbs et al. (1997). Using available information on aerosol optical properties (backscattered fraction, change in mass scattering efficiency with relative humidity, scattering optical depth, and absorption optical depth), Penner et al. estimate the direct mean global net radiative forcing of biomass burning aerosols to be 0.8 W m^{-2}. The Intergovernmental Panel on Climate Change (IPCC) (1995) later reduced this value by a factor of 4 due to the various approximations used by Penner et al. The value now reported by the IPCC for the direct effect of aerosol radiative forcing is -0.27 W m^{-2}. Hobbs et al. (1996) used data from the Smoke/Sulfate Clouds and Radiation experiment (McDougal 1995) held in 1995 over the Amazon basin and obtained optical properties for biomass burning. Using these new optical property values and keeping the other assumptions the same as Penner et al. yields a net radiative forcing value of about -0.27 W m^{-2}. The wide range in the net radiative forcing values for these studies is an indicator of the uncertainties associated in obtaining the radiative impact of aerosols.

We take a different approach to obtain the radiative forcing of aerosols that is similar to the cloud radiative forcing concept (see Ramanathan et al. 1989; Hartmann et al. 1986; Ackerman and Inoue 1994). In this method, narrowband measurements from the AVHRR are used to identify the smoke from biomass burning. Then, collocated measurements from the Earth Radiation Budget Experiment (ERBE) scanner are used to determine the top-of-the-atmosphere (TOA) fluxes for both clear-sky and aerosol regions. The difference between the clear and aerosol regions in the shortwave and longwave parts of the spectrum provide the ''shortwave aerosol radiative forcing'' and ''longwave aerosol radiative forcing,'' respectively. A recent study (Christopher et al. 1996) used a similar approach for a limited set of images (11) to obtain radiative forcing values. These values are called ''instantaneous radiative forcing values'' because they are obtained during the time of the satellite overpass. To obtain a global mean value, sufficient spatial and temporal sampling must be available. The Cloud and the Earth's Radiant Energy System/Visible Infrared Scanner (CERES/VIRS) combination of instruments that is available from the Tropical Rainfall Measuring Mission (TRMM) platform is especially suited for obtaining global means of aerosol radiative forcing because the tropical regions will be sampled several times during any given day. These estimates can then provide the necessary validation for both GCMs and radiative transfer studies.

The present study extends the previous work by Christopher et al. (1996). Fifty AVHRR images from the 1985 biomass burning season (August–October) are used to study the spatial and temporal distribution of fires as a function of four major ecosystems over South America. Two different fire detection schemes are presented. The regional radiative forcing of smoke aerosols are also presented as a function of ecosystems. Finally, error estimates are presented along with complete tables that characterize the narrowband and broadband properties of clear sky and smoke.

2. Datasets, preprocessing methods, and region of study

The AVHRR LAC images from *NOAA-9* are used in this analysis to map fires and smoke as a function of four major ecosystems. The period of study is from August to October 1985. Only daytime images during the ascending orbit (1430 LST) are used. Table 1 shows the list of images used with other pertinent information. The ERBE scanner (Kopia 1986), which was operational between February 1985 and January 1987 on *NOAA-9,* is used to obtain the radiative fluxes at the TOA.

The AVHRR provides images in five spectral channels at a ground spatial resolution of 1.1 km $\times$ 1.1 km at nadir. However, due to the large swath width (2700 km) at the edge of the scan, the ground resolution is 2.4 km $\times$ 6.9 km. The *NOAA-9* visible (0.58–0.68 μm) and near-infrared channels (0.725–1.1 μm) provide information on surface characteristics (e.g., Townshend et al. 1987) along with smoke loading (Kaufman and Nakajima 1993). The channel between 3.55 and 3.93 μm is well suited to provide information on fires both during night (Langaas 1992) and day (e.g., Belward et al. 1994) while the infrared channels (10.3–11.3 μm; 11.5–12.5 μm) provide information on surface temperature (Price 1984; McClain 1989). The infrared channels (channels

TABLE 1. List of images used in the study.

Number	Year	Month	Day	Satellite ID	Long (°)		Lat (°)		Start time GMT	End time GMT	Number of lines
					Min	Max	Min	Max			
1	1985	08	01	*NOAA-9*	−87.65	−54.46	−22.54	7.62	19.2714	19.3975	2728
2	1985	08	02	*NOAA-9*	−85.96	−53.09	−18.39	11.57	19.1114	19.2367	2699
3	1985	08	03	*NOAA-9*	−83.27	−50.16	−19.03	11.58	18.9278	19.0564	2777
4	1985	08	05	*NOAA-9*	−75.69	−35.91	−41.06	1.63	18.8400	19.0267	4035
5	1985	08	06	*NOAA-9*	−71.64	−42.10	−18.77	−3.33	18.3883	18.4428	1171
6	1985	08	07	*NOAA-9*	−72.46	−39.33	−18.91	11.73	18.2075	18.3358	2779
7	1985	08	08	*NOAA-9*	−69.76	−36.62	−18.89	11.75	18.0272	18.1558	2783
8	1985	08	09	*NOAA-9*	−63.59	−33.94	−18.73	−2.96	17.8475	17.9039	1219
9	1985	08	10	*NOAA-9*	−64.36	−31.19	−18.87	11.79	17.6667	17.7956	2783
10	1985	08	15	*NOAA-9*	−76.34	−43.12	−18.77	11.73	18.4672	18.5953	2768
11	1985	08	16	*NOAA-9*	−73.64	−40.41	−18.76	11.75	18.2869	18.4150	2770
12	1985	08	17	*NOAA-9*	−70.93	−37.65	−18.84	11.77	18.1064	18.2350	2779
13	1985	08	19	*NOAA-9*	−90.01	−56.46	−22.77	7.84	19.4283	19.5567	2778
14	1985	08	20	*NOAA-9*	−87.31	−53.74	−22.78	7.86	19.2481	19.3767	2780
15	1985	08	21	*NOAA-9*	−85.57	−52.31	−18.71	11.58	19.0872	19.2144	2473
16	1985	08	22	*NOAA-9*	−78.48	−49.59	−18.74	−7.78	18.9069	18.9394	706
17	1985	08	23	*NOAA-9*	−79.38	−46.91	−18.55	8.59	18.7275	18.8394	2416
18	1985	08	24	*NOAA-9*	−77.52	−44.23	−18.45	11.77	18.5478	18.6744	2741
19	1985	08	29	*NOAA-9*	−88.48	−54.75	−22.69	7.82	19.3272	19.4556	2770
20	1985	08	30	*NOAA-9*	−85.08	−53.27	−18.86	4.97	19.1658	19.2614	2062
21	1985	08	31	*NOAA-9*	−84.08	−50.80	−17.98	11.70	18.9897	19.1139	2685
22	1985	09	01	*NOAA-9*	−80.56	−47.85	−18.75	8.57	18.8056	18.9183	2437
23	1985	09	02	*NOAA-9*	−78.69	−45.07	−18.87	11.75	18.6247	18.7536	2783
24	1985	09	03	*NOAA-9*	−75.98	−42.84	−17.25	11.80	18.4525	18.5736	2619
25	1985	09	04	*NOAA-9*	−73.25	−39.62	−18.86	11.73	18.2642	18.3928	2780
26	1985	09	05	*NOAA-9*	−70.54	−36.92	−18.84	11.69	18.0842	18.2125	2775
27	1985	09	06	*NOAA-9*	−67.85	−34.19	−18.79	11.74	17.9042	18.0325	2775
28	1985	09	07	*NOAA-9*	−89.65	−55.83	−22.38	7.83	19.4078	19.5344	2736
29	1985	09	10	*NOAA-9*	−77.39	−39.05	−42.36	−11.74	18.7700	18.8975	2757
30	1985	09	10	*NOAA-9*	−82.52	−48.79	−18.89	11.71	18.8839	19.0128	2777
31	1985	09	11	*NOAA-9*	−79.71	−46.04	−18.93	11.34	18.7036	18.8306	2748
32	1985	09	12	*NOAA-9*	−71.99	−40.86	−26.21	−11.66	18.4881	18.5372	1069
33	1985	09	12	*NOAA-9*	−72.79	−43.33	−18.89	−7.32	18.5236	18.5589	758
34	1985	09	13	*NOAA-9*	−74.39	−40.58	−18.91	11.70	18.3431	18.4719	2783
35	1985	09	15	*NOAA-9*	−93.46	−59.38	−22.84	7.74	19.6650	19.7933	2779
36	1985	09	16	*NOAA-9*	−90.73	−56.78	−22.49	7.69	19.4864	19.6131	2737
37	1985	09	17	*NOAA-9*	−58.40	−19.71	−42.75	−11.91	17.5061	17.6347	2776
38	1985	09	17	*NOAA-9*	−87.98	−53.97	−22.73	7.52	19.3050	19.4319	2745
39	1985	09	19	*NOAA-9*	−83.57	−49.70	−19.10	11.47	18.9622	19.0908	2776
40	1985	09	20	*NOAA-9*	−75.78	−37.05	−42.79	−12.05	18.6664	18.7947	2772
41	1985	09	24	*NOAA-9*	−64.97	−26.18	−42.69	−11.82	17.9458	18.0744	2780
42	1985	09	24	*NOAA-9*	−70.02	−36.11	−19.06	11.50	18.0608	18.1894	2780
43	1985	09	24	*NOAA-9*	−94.55	−60.34	−22.98	7.65	19.7431	19.8719	2775
44	1985	09	25	*NOAA-9*	−62.26	−23.48	−42.65	−11.87	17.7658	17.8942	2759
45	1985	09	25	*NOAA-9*	−67.28	−33.38	−19.03	11.49	17.8808	18.0092	2774
46	1985	09	25	*NOAA-9*	−90.55	−57.61	−22.99	2.19	19.5631	19.6650	2199
47	1985	09	26	*NOAA-9*	−59.55	−20.93	−42.34	−11.84	17.5869	17.7139	2744
48	1985	10	02	*NOAA-9*	−67.86	−33.19	−36.36	−17.48	18.2358	18.3056	1506
49	1985	10	04	*NOAA-9*	−92.80	−58.58	−23.28	7.31	19.6406	19.7692	2778
50	1985	10	22	*NOAA-9*	−65.28	−26.35	−43.12	−12.31	17.9994	18.1281	2781

4 and 5) have an onboard calibration source, while channels 1 and 2 are calibrated only before launch. Therefore, the degradation of the visible and near-infrared sensors in orbit are taken into account using the methodology described in Rao et al. (1993a). Nonlinear calibration of the thermal channels are computed following Rao et al. (1993b). The 3.7-μm channel (channel 3) contains both an emitted and a reflected portion. The thermal portion is removed using the AVHRR channel 4 temperatures, and the reflectance in channel 3 is computed using standard techniques (Allen et al. 1990; Kaufman and Nakajima 1993).

The ERBE scanner measured broadband radiances at the TOA in the shortwave (0.25–4 μm) and longwave (4–50 μm) portions of the electromagnetic spectrum (Kopia 1986). Considering the point spread function, the ERBE scanner on *NOAA-9* had a nadir ground resolution of about 35 km × 35 km. Both the shortwave and longwave channels are well calibrated both before launch and during the lifetime of the instrument (Bark-

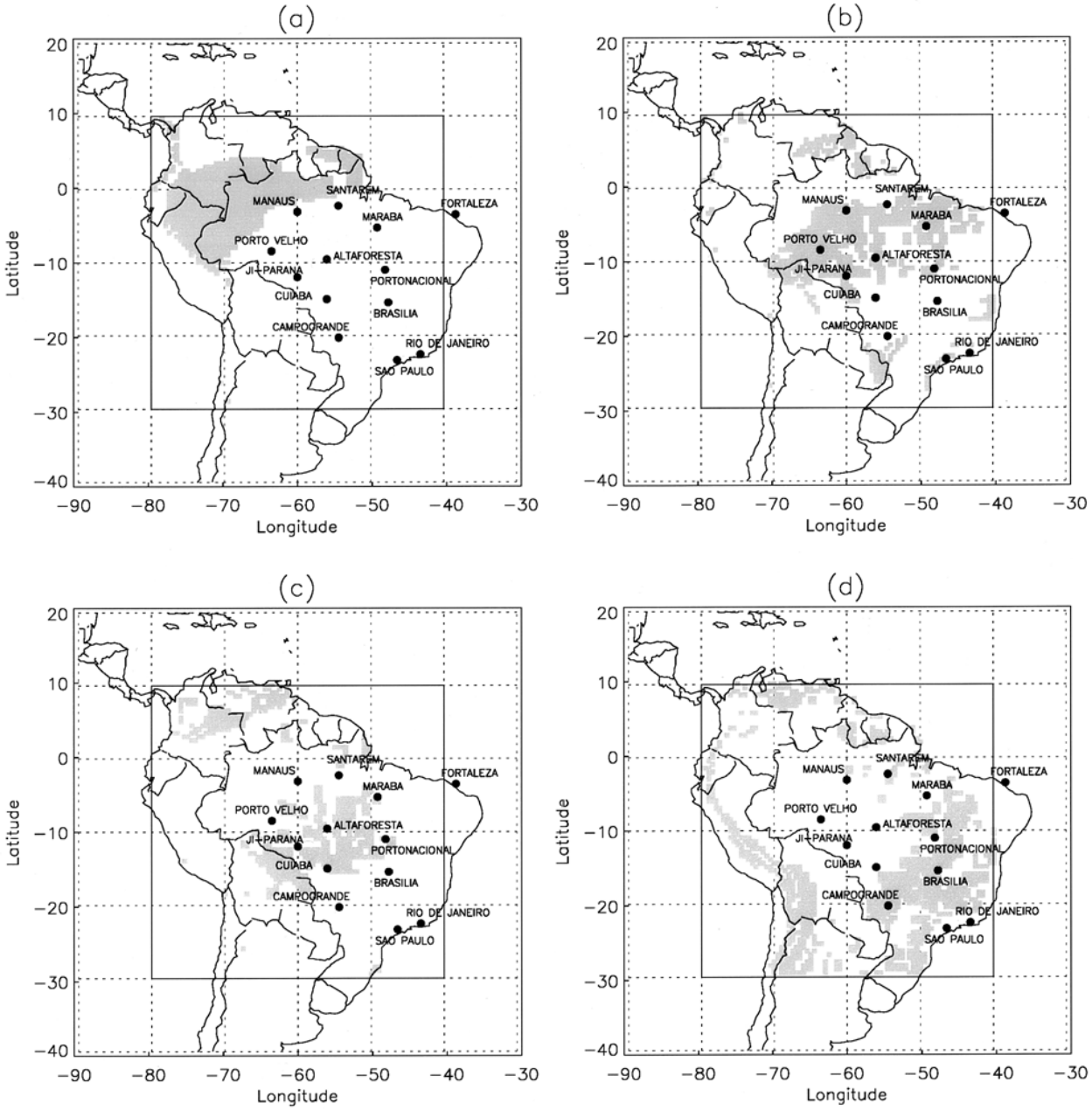

FIG. 1. Region of study (outlined in the rectangle) and four major ecosystems within South America: (a) tropical rain forest (TRF), (b) tropical broadleaf seasonal (TBS), (c) savanna/grass/seasonal woods (SGW), and (d) mild/warm/hot grass/shrub (MGS).

strom 1984). The radiances are converted to TOA fluxes using a maximum likelihood classifier (Wielicki and Green 1989) and angular directional models (ADMs) (Suttles et al. 1988; Suttles et al. 1989).

The region of study shown in Fig. 1 in the enclosed rectangle between 10°N to 30°S and 40° to 80°W encompasses four major ecosystems within South America. The four ecosystems (Olson 1991) are 1) tropical rain forest (TRF) (Fig. 1a), 2) tropical broadleaf seasonal (TBS) with dry or cool season (Fig. 1b), 3) savanna/grass and seasonal woods (SGW) (Fig. 1c) (note that in this category, trees or shrubs above grass ground cover may be interspersed in many scales in savanna belts of varying drought duration and high fire frequency), and 4) mild/warm/hot grass shrub (MGS) (Fig. 1d). Also shown in this figure are selected sites of interest. Porto Nacional, which is located on the eastern side of the Amazon basin, is a cerrado region that is categorized by the Olson database as MGS. The natural vegetation in this ecosystem is routinely cleared for agricultural purposes. Cuiaba, located in the state of Matto Grasso, is characterized as SGW and is also a region

of agricultural cultivation. Alta Foresta is categorized as a tropical broadleaf seasonal forest and has experienced rapid intense biomass burning in the past. Holben et al. (1996) describe the sun-photometer network at these various sites. Manaus and Santarem, located on the main Amazon, experience very little biomass burning, and Ji-Parana, located in Rondonia, experiences fires from primary forest clearing, secondary growth, and grass fires.

3. Methodology

a. Identifying clear-sky regions using the pairwise-histogram approach

The pairwise-histogram classifier is currently being developed as part of the Clouds and the Earth's Energy System (CERES) global cloud and aerosol identification efforts (Baum et al. 1996). The main purpose of this algorithm is to use existing AVHRR 1-km Pathfinder (Eidenshink and Faundeen 1994) data and to develop a product that will label each pixel into one of 23 classes in an automated fashion. This algorithm is directly applicable for the Visible Infrared Scanner (VIRS) instrument on the TRMM platform since the AVHRR and VIRS have similar spectral and spatial resolution characteristics.

The calibrated, preprocessed AVHRR images are first used to manually identify several classes: 1) water, 2) land, 3) snow, and 4) water cloud over land, etc. Then a total of 185 features [(a) five calibrated pixel values of AVHRR channels 1–5 and channel 3 reflectances, (b) channel differences, and (c) channel ratios, etc.] are calculated for use in the pairwise-histogram classifier. The goal of the paired-histogram classifier is to find a set of features for each pair of classes that provides optimal separation. Within each feature, histograms are created for the classes. The histograms of each pair of classes are compared and two measures, namely, overlap and divergence, are computed. This process is repeated for each feature and for each pair of classes; the features are sorted by the smallest overlap. The features with equal overlaps are sorted by the largest divergence value. In the current study, this algorithm is used to identify only clear-sky pixels (without clouds and smoke) and the reason for using this algorithm is the in-house availability.

b. Fire detection

The detection of fires from AVHRR imagery is a well-established procedure (see Kaufman and Justice 1994 for a comprehensive review). The physical principle behind the detection of fires from AVHRR imagery is the increased 3.7-μm channel response to fires when compared to the background. Robinson (1991) defines the amplification factor as the ratio of fire irradiance to the background irradiance. Calculations show that at 3.7 μm, amplification factors of about 3200 and 20 000 are predicted for cool (1000 K) and hot fires (1800 K), which make the detection of fires possible from satellite imagery. However, it is noted that fires saturate the AVHRR sensor (the maximum detectable temperature by the *NOAA-9* 3.7-μm channel is 319 K) and hot bare soils could be confused with active fires. In spite of these limitations, the AVHRR is the only instrument that is routinely used to obtain fire counts over several regions of the earth.

The most widely used fire detection scheme that is applicable over the Amazon was developed by Kaufman et al. (1990). In this method, a pixel is classified as fire if the following three conditions are met. The first condition ($T3 \geq 316$, where $T3$ is the AVHRR channel 3 temperature) ensures that the channel 3 temperatures are close to the saturation level. The second condition ($T3 \geq T4 + 10$, where $T4$ is the AVHRR channel 4 temperature) ensures that the hot bare soils are not classified as fire pixels. The third condition ($T4 \geq 250$ K) ensures that reflective bright clouds are not identified as fire pixels. We modified one of these thresholds slightly to suit this study (instead of $T4 \geq 250$ K, the threshold was changed to $T4 \geq 273$ K). This modification is a conservative estimate for screening clouds. We call this fire detection scheme MKF, which stands for modified Kaufman et al. algorithm. In the current study, the MKF scheme is compared to a fire detection scheme that utilizes the results of the paired-histogram classifier and several spatial and spectral conditions (Kaufman and Justice 1994). For pixels classified as clear land (desert ecosystems and water bodies are eliminated using the Olson ecosystem map) with no sun glint contamination, a series of contextual tests are performed. For a 10×10 group of clear-sky pixels, within a view angle of 45°, if $T3 \leq 315$ and if $T3 - T4 \leq 8$ K, no fires are detected. Then $T3$ and $T4$ are corrected for water vapor effects similar to Prins and Menzel (1994). For the TRF ecosystem, the infrared temperatures are adjusted by 4 K, and for the other three ecosystems (TBS, SGW, and MGS), the infrared temperatures are adjusted by 2 K for water vapor absorption. These assumptions are also well supported by the TIROS Operational Vertical Sounder (TOVS)-measured surface skin temperature values, as discussed in the results section. Strong fires are characterized as $T3 - T4(T_{34}) > 15$ K and $T4 > 319$ K. Then, using the thresholds outlined in Kaufman and Justice (1994), further analysis is performed that identifies a pixel as fire or nonfire. Pixels are defined as fire if the following conditions are met:

$$T3 > T_{3b} + 2\delta T_{3b} \quad \text{or} \quad T3 > 319 \text{ K}$$

and

$$T_{34} > \Delta T_{34b} + 2\delta T_{34b} \quad \text{or} \quad T_{34} > 20 \text{ K}, \qquad (1)$$

where

$T3$ = AVHRR channel 3 temperature,

$T4$ = AVHRR channel 4 temperature,

T_{3b} = AVHRR channel 3 temperature of the background,

ΔT_{34} = channel 3 − channel 4 temperatures,

ΔT_{34b} = channel 3 − channel 4 temperatures for the background pixels, and

δT_{34b} = standard deviation of channels 3 and 4 temperatures for the background.

The basic idea behind this algorithm is to detect fires if

1) the channel 3 temperature of a pixel is greater than the channel 3 temperature of the background plus two times its standard deviation or if channel 3 temperatures is greater than 319 K, and
2) the difference in channel 3 and channel 4 temperatures is greater than the background temperature difference plus two times the standard deviation. This fire detection scheme is called EBAF (Ecosystem Based Fire Detection) for notational simplicity and is a modification of the algorithm described by Kaufman and Justice (1994).

A similar algorithm is used by Justice et al. (1996) to detect fires over Africa. Flasse and Ceccato (1996) also describe a similar algorithm that could be used on a global basis. It is noted that this is the beginning of an effort to develop an algorithm that could be used on a global basis. Future developments will include 1) correction for water vapor effects using the TOVS database, 2) emissivity corrections based on available data, and 3) extensive ground-based validation.

c. Collocation of AVHRR with ERBE data and smoke identification

The AVHRR and ERBE are precisely collocated in time because both the instruments obtained data from *NOAA-9*. However, the spatial resolution of ERBE is much larger than that of the AVHRR. Therefore, a group of (35 × 35) AVHRR pixels that correspond to an ERBE footprint is identified by matching the ERBE latitude and longitude with that of the AVHRR. Collocation accuracies are checked by computing linear correlation coefficients between AVHRR channel 4 temperatures and ERBE longwave (LW) fluxes along with AVHRR channel 1 reflectances with ERBE shortwave (SW) fluxes. Typical correlation coefficients are greater than 90%.

Smoke pixels are identified by first locating fires within a collocated ERBE pixel. Within an ERBE pixel if fire and/or fires are present, then each AVHRR pixel is checked to ensure if the channel 4 temperatures are warmer than 273 K. If this criteria is satisfied, then the ERBE pixel is classified as a ''smoke pixel.'' This method captures the smoke directly above the fires that are warmer than 273 K. Although it is possible to include clouds in this method, a visual examination of several images shows that directly above the fires, smoke predominates, as opposed to low-level water clouds. This method of identifying smoke does not differentiate the magnitude of the smoke optical depth, which can vary over a wide range, depending upon the site fuel loading, the duration of the fires, and the level of background smoke from other fires.

d. Radiative forcing of smoke

The concept of radiative forcing using broadband measurements are described in a series of papers that utilize the ERBE data [e.g., Ramanathan et al. 1989; Hartmann et al. 1986]. However, most of these studies were applied to studying clouds on a global scale. Only a very few studies have utilized ERBE measurements to estimate the impact of aerosols. Ackerman and Chung (1992) used ERBE measurements for seven images to estimate the difference in SW and LW fluxes at the TOA for aerosols produced by dust storms, although no radiative forcing estimates were provided. Minnis et al. (1993) used broadband wide field of view measurements monthly mean Earth Radiation Budget Satellite (ERBS) measurements to estimate the radiative impact of volcanic aerosols from the Mount Pinatubo eruption. The concept of radiative forcing is to determine if either clouds or aerosols ''warm'' or ''cool'' the earth. The following radiative forcing terms expressed in watts per square meter are defined as follows:

$$\text{shortwave radiative forcing (SWARF)} = S_0[\alpha_{\text{clr}} - \alpha_{\text{aer}}], \tag{2}$$

where

S_0 = incoming solar flux,

α_{clr} = clear-sky albedo, and

α_{aer} = aerosol-sky albedo;

$$\text{longwave radiative forcing (LWARF)} = \text{LW}_{\text{clr}} - \text{LW}_{\text{aer}}, \tag{3}$$

where

LW_{clr} = clear-sky longwave flux at the TOA, and

LW_{aer} = aerosol longwave flux at the TOA;

and

$$\text{net radiative forcing (NETARF)} = \text{SWARF} + \text{LWARF}. \tag{4}$$

If shortwave radiative forcing is negative, then it denotes a cooling effect because aerosols reflect more of

the incoming solar radiation than clear-sky regions. If longwave radiative forcing is positive, then it denotes warming effect because even in the presence of aerosols, the outgoing longwave radiation for clear sky is larger than that of aerosols. The NETARF, therefore, is the sum total of these two effects. If NETARF is negative, then it means that the influence of aerosols on the regional radiative balance is one of cooling. If NETARF is positive, it denotes a warming effect where the effect of aerosols warms the earth–atmosphere system.

The radiative forcing terminology defined this way are called ''instantaneous radiative forcing'' because no space or time averages have been performed. Throughout this paper, the radiative forcing that is referred to is instantaneous radiative forcing, unless it is stated otherwise. The ideal method to obtain the temporally averaged global mean radiative forcing values for aerosols is to 1) properly identify the aerosols from narrowband sensors (such as the AVHRR, VIRS, MODIS) and 2) to replace the α_{aer} and LW_{aer} by α_{obs} and LW_{obs}, respectively, where α_{obs} and LW_{obs} denote observed albedo and observed LW flux from broadband measurements, respectively (Ramanathan et al. 1989), and to further quantify the aerosol radiative effects as a function of smoke optical depth. The observed values could be 1) clear sky, 2) cloudy, or 3) aerosols. Note that a combination of these is also possible. When averaged over a day and month (Barkstrom 1984), we can then obtain global aerosol radiative forcing estimates, provided adequate number of measurements over a given region are made. With a polar orbiting satellite, only two measurements can be made over a given area in the Tropics. Traditionally, a combination of two polar orbiting satellites are available for any time period (e.g., *NOAA-9* and *NOAA-10* for the current study). Even with two polar orbiting satellites, a given area in the Tropics will be observed four times a day, two of which will be during hours when no sunlight or when minimum sunlight is available. To circumvent this problem, coincident narrowband and broadband measurements must be made from a low-orbit satellite in a precessing orbit with respect to the sun that will enable sufficient diurnal sampling of a given area. This type of orbit can sample all local times over the course of a month (Kidder and Vonder Haar 1995). Although ERBS was positioned in such an orbit, no narrowband radiometers were available from this satellite. However, the TRMM platform, in a precession orbit, carries a narrowband radiometer (VIRS) and a broadband scanner (CERES), which is well suited to obtain global estimates of temporally averaged aerosol radiative forcing.

4. Results and discussion

Figure 2 shows a series of AVHRR images from 1–6 September 1985. These images are approximately centered around 10°S and 60°W. The latitude and longitude for the northwest, northeast, southeast, and southwest corners for the images are shown in Table 2. This figure is a typical three-band overlay that is used to highlight the various features. The AVHRR channel 1 is in red, the ''mean'' textural measure (Christopher et al. 1996) of channels $(1 - 4)/(1 + 4)$ is blue, and the normalized channel combination of $(1 - 4)/(1 + 4)$ is in green. The combination of spectral and textural information has been useful in visually separating smoke and clouds from the underlying background. The dark areas are clear-sky regions, the light yellow color that is seen on all the images is the optically thin haze that is found throughout the biomass burning season (Andreae et al. 1988), and the bright yellow color shows the dense smoke plumes. Most of these dense plumes are associated with fires that are apparent in these images. The blue color denotes the water clouds and the white color shows clouds with cloud-top temperatures colder than 273 K. Several interesting features can be seen from these images. On 1 September 1985, the image is mostly cloud covered with only a very few fires seen in Rondonia. On 2 September Rondonia is relatively clear with many fires toward the center of the image. On 3 September 1985 there is a classic image with a dense smoke plume in Rondonia that has several active fires, and a major portion of the image is covered with smoke haze. On 4 September, the dense smoke plume is no longer apparent, but there are a large number of fires. On 5 September 1985, Rondonia is toward the western edge of the image, but a large number of fires with several smoke plumes are visible. On 6 September 1985, the image shows the large number of fires to the southeast of Rondonia. Figure 2 is a good example of the fire activities and the associated smoke that are prevalent during the biomass burning season. The fires are usually categorized into flaming and smoldering fires (Ward et al. 1992), although it is difficult to precisely distinguish between the two types from current satellite imagery. Flaming conditions exist for a short period of time, during the start of the fires, with high combustion efficiencies and low emissions of gases and particles. Smoldering conditions, on the other hand, release large amounts of trace gases and have a lower combustion efficiency. Given the fact that most of the observed fires by the AVHRR are not during the time of ignition, the fires seen in Fig. 2 are probably from the smoldering phase.

Figure 3 shows the temporal distribution of fires for all images that were analyzed for the four ecosystems for August, September, and October 1985. The solid histograms denote the fires detected by the MKF method, and the clear histograms denote the fires detected by the EBAF method. The TRF has few fires in August, while the other three ecosystems (TBS, MGS, and SGW) have maximum fires of about 5000 during the middle of the month. The EBAF and MKF methods compare well for the month of August, with the MKF method detecting more fires on certain days (e.g., 10 August). The EBAF method is probably a conservative

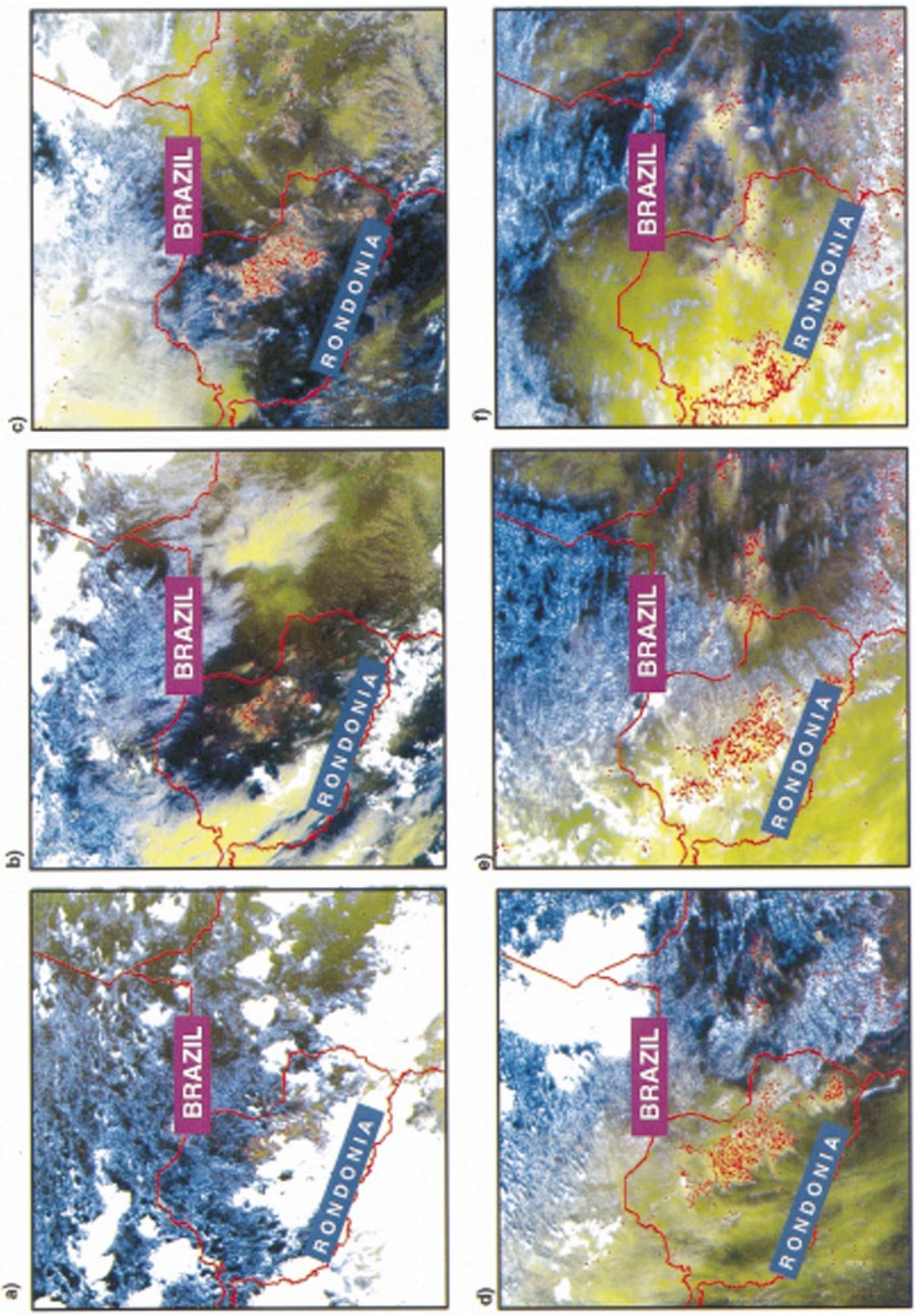

FIG. 2. AVHRR images from (a) 1 September 1985, (b) 2 September 1985, (c) 3 September 1985, (d) 4 September 1985, (e) 5 September 1985, and (f) 6 September 1985. The red dots denote fires, the light yellow color the haze, and the bright yellow color the dense smoke; the clouds with cloud-top temperatures colder than 273 K are assigned the color white.

TABLE 2. Latitudes and longitudes for images in Fig. 2.

	NW		NE		SE		SW	
Day	Lat	Long	Lat	Long	Lat	Long	Lat	Long
1 Sep	8°S	65°W	7°S	57°W	14°S	55°W	17°S	63°W
2 Sep	8°S	62°W	7°S	54°W	15°S	52°W	16°S	60°W
3 Sep	6°S	59°W	5°S	52°W	12°S	50°W	14°S	58°W
4 Sep	8°S	56°W	7°S	49°W	15°S	47°W	16°S	55°W
5 Sep	8°S	54°W	7°S	46°W	15°S	44°W	16°S	52°W
6 Sep	8°S	51°W	7°S	44°W	14°S	42°W	16°S	49°W

estimate since more spectral and spatial tests are performed to eliminate false signals. During September, the TRF has very few fires and the majority of the fire activities are in the TBS, MGS, and the SGW ecosystems. There is a well-defined temporal variation in fire activities that may be in part due to cloud cover variations where fires cannot be detected. In the TBS and MGS areas, fire activities are concentrated in the first 15 days, whereas in the SGW areas, fire activities persist throughout the month. The summary in Table 3 shows the comparison between the two methods for the four ecosystems. MKF > EBAF denotes the number of days when the MKF method detected more fire pixels than the EBAF method. For example, the MKF method overestimated fire counts on 27 days in the SGW ecosystem when compared to the EBAF technique. The statistics for the TRF ecosystem, as shown in Table 3, must be interpreted with caution because less than 1% of the total number of fires were detected in this ecosystem. These statistics show that for the TBS ecosystem, the MKF technique underestimates fire counts, relative to the EBAF technique, whereas for the MGS and SGW ecosystems, the MKF method overestimates fire counts 60%–70% of the time. The reason for this overestimation could be due to the warmer background temperatures misidentified as fire pixels since the surface temperatures in the MGS and SGW ecosystems are higher than the TBS and TRF ecosystems. For the TBS ecosystem, the maximum underestimation of fire counts are on the order of 15%–25%. For example, on 2 September 1985, the MKF method detected 819 fire pixels, and the EBAF method detected 993 fire pixels, thereby leading to an underestimation of about 21%. On the other hand, the MKF method overestimates fire counts significantly for the MGS and SGW ecosystems on certain days. For example, on 24 September 1985, the MKF method overestimates fire counts by about 60%. A visual examination of the images showed that there were many pixels falsely identified as fires by the MKF method along the coastal regions of South America. The EBAF method that utilizes spatial, spectral, and ancillary databases appears to perform well over the entire study area and is assumed as ''truth'' in this discussion. The number of fires and their temporal distribution of fires compares well with previous studies (Kaufman et al. 1990; Setzer and Perreira 1991). Fire activities are intense in September with a majority of fires occurring in the MGS and SGW ecosystems.

During August, September, and October 1985, a total of 211 580 fires were detected in all four ecosystems by the EBAF method. Out of these, less than 1% of the fires were detected in the TRF. The percentage of fires detected for the TBS, MGS, and SGW ecosystems were 27%, 32%, and 40%, respectively. These results indicate that the majority of the fires are related to agricultural practices. Note that the exact fire counts do have limitations, as outlined in Robinson (1991).

Figure 4 shows the frequency histogram of shortwave fluxes for clear-sky and smoke regions. Figures 4a–d are clear-sky SW fluxes for the four ecosystems; Figs. 4e–h, the SW fluxes for smoke. The SW fluxes for clear-sky regions range between 140 and 180 W m^{-2} with peak clear-sky SW fluxes between 150–160 W m^{-2} for TRF and SGW, and between 160 and 170 W m^{-2} for TBS and MGS. The SW fluxes for smoke, on the other hand, are larger than those of clear-sky regions for all four ecosystems with some overlap between 160 and 180 W m^{-2}. On the average, the smoke aerosols have a larger SW flux than those of clear-sky regions. Note the large variability in the smoke SW fluxes, which is due to the wide range of aerosol optical depth in these cases. The SW flux values for smoke range between 160 and 250 W m^{-2}. The distribution of smoke SW fluxes appears rather uniform for the MGS and SGW ecosystems and are larger than those of the corresponding clear-sky regions. The peak SW flux values for the TBS are between 170 and 200 W m^{-2}, an approximate increase of about 40–50 W m^{-2} from the clear-sky regions. For the TBS, MGS, and SGW ecosystems, there is a wide range of SW flux values with peak values between 160 and 180 W m^{-2}.

Figure 5 shows the LW flux values for the clear-sky and the smoke regions. Unlike the clear-sky SW flux values, the LW values show a well-defined trend between the four ecosystems. The TRF ecosystem has peak clear-sky LW fluxes between 270 and 280 W m^{-2}, whereas the TBS shows peak values between 290 and 300 W m^{-2}. The SGW, peak clear-sky LW fluxes are between 300 and 310 W m^{-2}, whereas the MGS ecosystem has the largest peak clear-sky values between 320 and 330 W m^{-2}. Although the peak values are different between the ecosystems, there is a wide range of LW fluxes among the four ecosystems, ranging between 260 and 330 W m^{-2}, which results from the difference in surface temperatures. The LW flux values indicate that the mean average temperatures are different from the TRF to the SGW ecosystems, a fact well supported by the TOVS-measured skin temperatures, as discussed later in the paper. For smoky regions the LW fluxes have peak values betwen 290 and 310 W m^{-2}. However, note that there is a large overlap between the LW flux values for clear-sky and smoke regions that shows the difficulty in separating the LW effects of smoke from the underlying background. Most of the smoke found

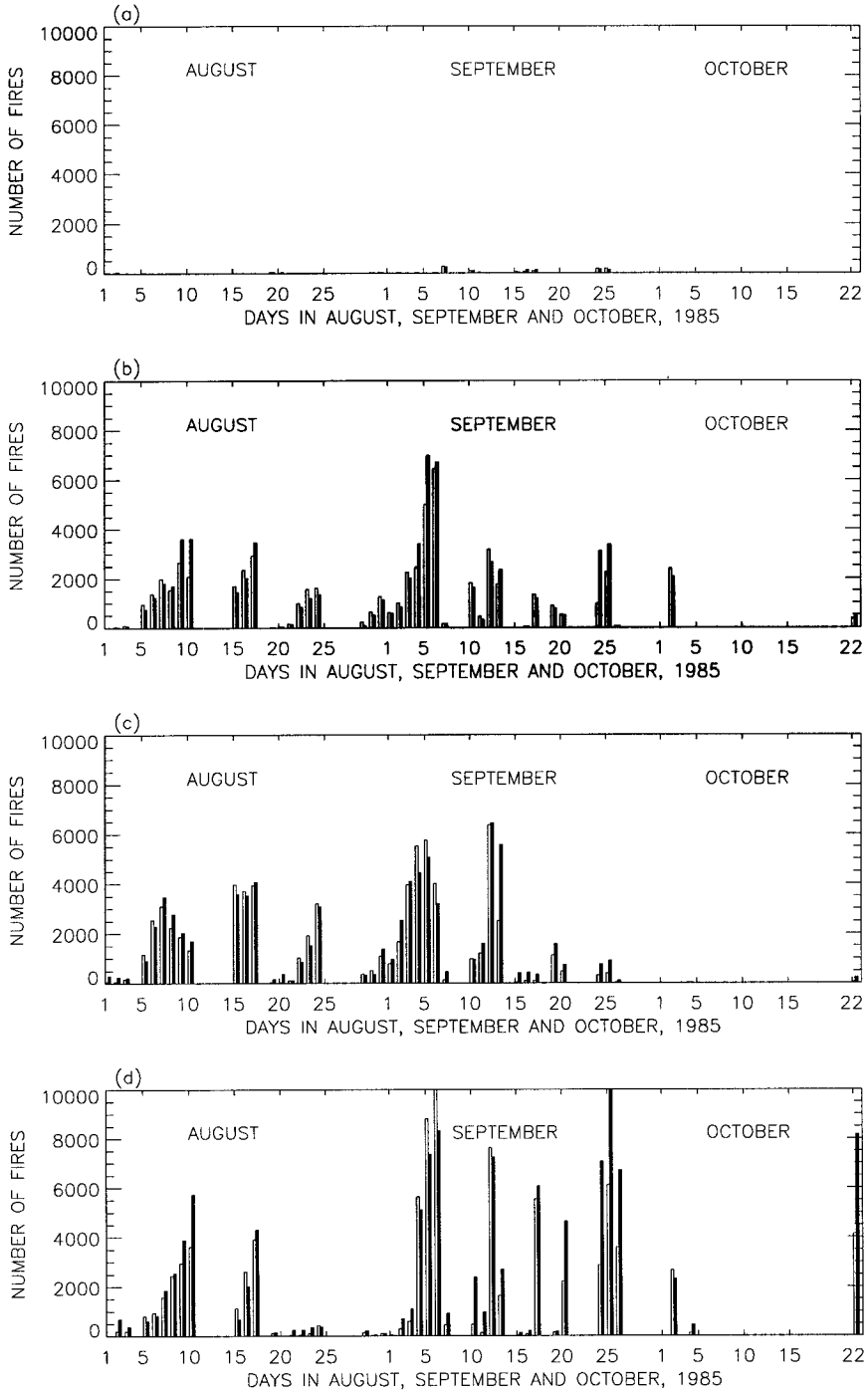

FIG. 3. Temporal distribution of fires for four ecosystems: (a) TRF, (b) TBS, (c) SGW, and (d) MGS during August, September, and October 1985. The solid histograms are from the MKF method and the clear histograms are from the EBAF method.

between 1 and 4 km in altitude (Anderson et al. 1996) have similar radiating temperatures when compared to the ground. Although the LW flux values are similar between the smoke and clear-sky regions, the difference in SW fluxes between clear-sky and smoke regions accounts for the negative net radiative forcing values, which implies a *cooling* effect.

Table 4 shows the mean and standard deviations of spectral and broadband properties for clear sky and smoke calculated from AVHRR and ERBE, respective-

TABLE 3. MKF and EBAF statistics for four ecosystems.

	MKF > EBAF	MKF = EBAF	MKF < EBAF
TRF	9	15	18
TBS	13	0	29
SGW	27	1	14
MGS	30	0	12

ly. These statistics are for August, September, and October 1985 and therefore are representative of the dry season in South America. Also shown in the table are monthly mean precipitation, water vapor, and surface skin temperature values from the TOVS Pathfinder dataset that are derived using the physical retrieval method of Susskind et al. (1984). These TOVS values are shown to highlight the meteorological conditions for these ecosystems. The TOVS data show that there is a well-defined change in precipitation, water vapor, and skin temperature among the four ecosystems. The TRF has higher precipitable water vapor (4.37 cm s^{-1}) and therefore higher precipitation (4.29 mm day^{-1}) when compared to all other ecosystems. The average temperature is also lower than the other four ecosystems due to the absorption of incident solar radiation by the thick canopy. However, note that this is the dry season in Amazonia. Typical rainfall rates and precipitable water are much higher during the wet season (November–May). Also note the clear-sky channel 4–5 (C45) temperatures, which are indicators of the water vapor content for clear-sky regions (Price 1984; Choudhury et al. 1995). Clear-sky C45 differences are maximum over TRF, with decreasing C45 values over the TBS, MGS, and SGW ecosystems. The skin temperature noted by TOVS is larger than the channel 4 temperatures measured at the TOA due to the water vapor amounts. Therefore, atmospheric corrections for channel 4 temperatures of about 4 K for TRF and 2 K for TBS, SGW, and MGS are representative for this area. Several interesting observations are made from Table 4. The tropical rain forest has the lowest clear-sky AVHRR channel 1 reflectances, the lowest AVHRR clear-sky infrared temperatures, and the lowest broadband ERBE LW fluxes due to the dense vegetation. Channel 3 reflectances for clear-sky regions vary between 4.3% and 5.8%, which is typical for the vegetation types in Amazonia. The broadband albedo varies from 14.6% to 16.4% for clear-sky regions, which is also characteristic for this area (Penner et al. 1992). The narrowband and broadband properties for smoke are different than those of clear-sky regions, as indicated by the bold numbers in Table 4. The mean channel 1 reflectances for smoke are about 19% (compared to 9%–10% for clear sky), with standard deviations on the order of 2%–3%. Channel 4 temperatures for ''smoky'' regions are very similar to those of the clear-sky regions that show, on average, that most of the smoke is near the surface. It is emphasized that these are average conditions for the entire study period. Channel 3 reflectances are also very low for the smoky regions because at near-infrared wavelengths, the aerosols do not reflect the incident radiation due to the small particle sizes. The broadband SW and LW flux values for smoke are smaller than those of clear-sky regions. On average, the SW fluxes of smoky regions are greater than those of clear-sky regions by about 20–30 W m^{-2}, while the LW fluxes are different by about 0–7 W m^{-2}. This shows that smoke aerosols have a larger effect on reflecting incoming solar radiation when compared to modulating the LW flux emitted by the earth–aerosol system. Once the clear-sky SW fluxes have been determined, the mean clear-sky SW and LW flux values for each ecosystem are then used to compute the radiative forcing terms. The uncertainties in assuming a single value for clear-sky fluxes are discussed in section 5c.

Table 5 shows the SWARF, LWARF, and NETARF values for the four ecosystems. The SWARF values for all four ecosystems are negative, ranging from −25.3 to −40.6 W m^{-2}. The TRF results should be interpreted with caution because very few smoke pixels were identified during the period of study. The negative values indicate that the smoke pixels on the average reflect more of the incoming solar radiation as opposed to clear-sky regions. These values are consistent with our previous study (Christopher et al. 1996). The mean LWARF values range from −0.3 to 6.7 W m^{-2}, with the MGS ecosystem having the only negative LWARF value. The NETARF, which is the sum of the SWARF and LWARF terms, therefore, shows the predominant effect of the reflective properties of smoke aerosols. The instantaneous net radiative forcing values are negative for all four ecosystems, with the TBS ecosystem having the largest NETARF values of about −35.3 W m^{-2}. These results show that the net radiative impact of aerosols for all four major ecosystems in South America is one of cooling.

5. Uncertainty factors

In this section, the various uncertainties associated with the estimation of radiative forcing are discussed. The following sources are identified.

a. Uncertainties in AVHRR and ERBE measurements

It is assumed that the preprocessing of the AVHRR data to account for 1) the degradation of the visible and near-infrared channels and 2) the nonlinear calibration of the infrared channels is adequate for this study. While the ERBE measurements were well calibrated before launch and during operation, the final data products are a combination of measured radiances and model computations. For instantaneous radiances, the uncertainties in longwave observations are about 1%, and the uncertainties in shortwave observations are about 2%–3% (Barkstrom et al. 1989). The ERBE-measured radiances are then inverted to TOA fluxes using a maximum like-

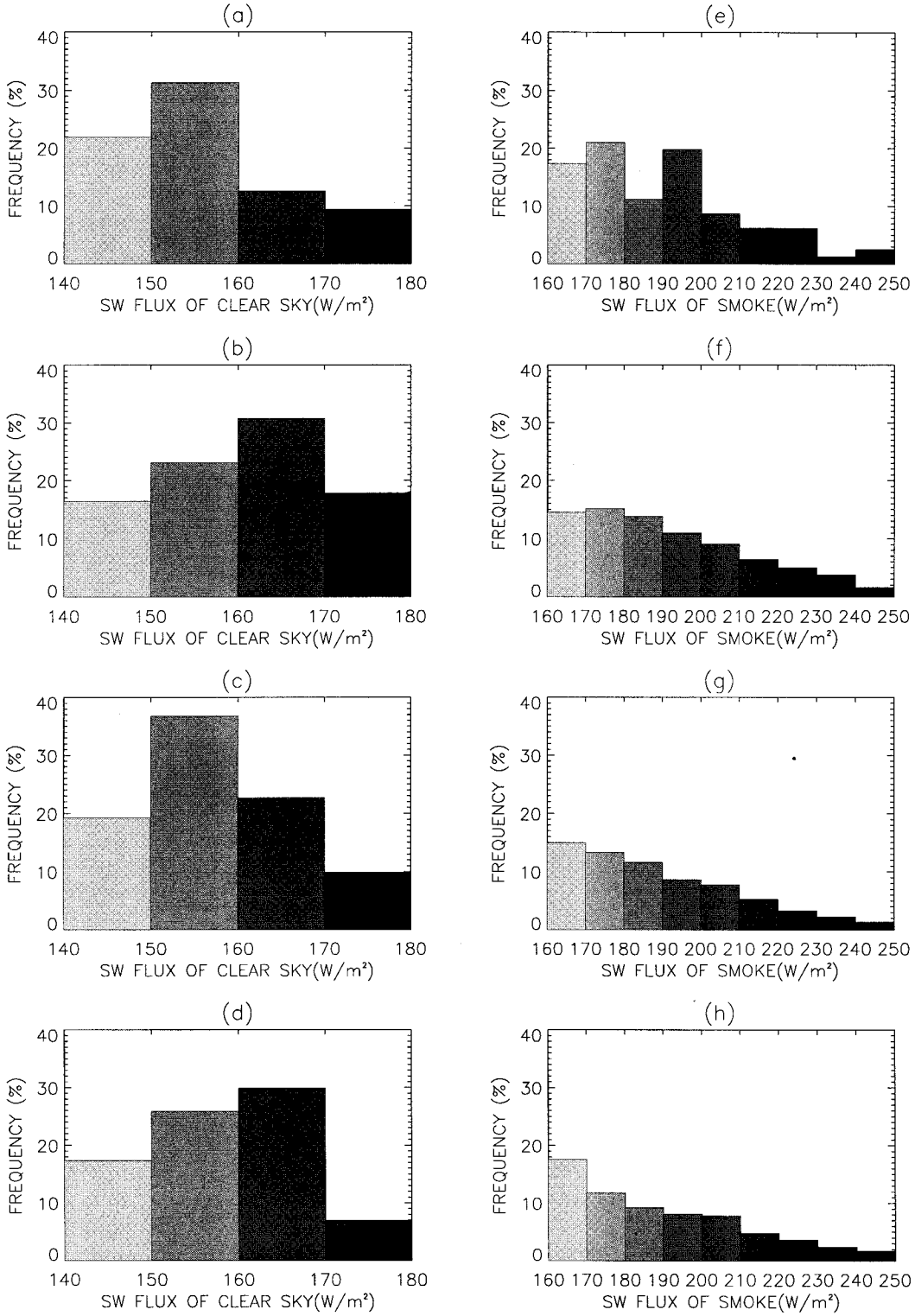

FIG. 4. Shortwave fluxes in watts per square meter for four ecosystems (TRF, TBS, SGW, and MGS): (a)–(b) clear-sky regions, (e)–(h) smoke.

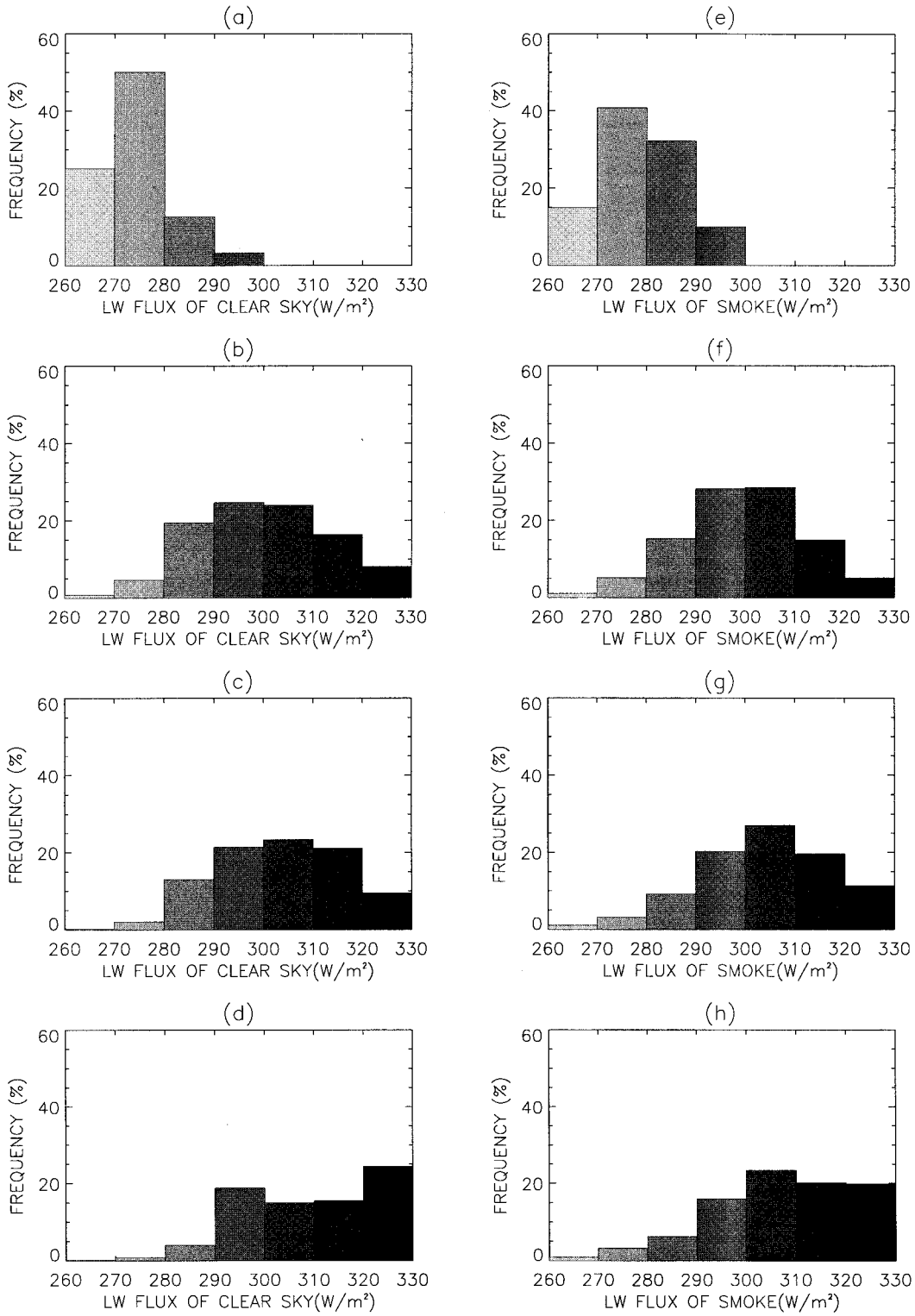

FIG. 5. Same as Fig. 4 except for longwave fluxes.

TABLE 4. Narrowband and broadband means and standard deviations for clear sky and smoke for four ecosystems.

		Tropical rain forest		Tropical broadleaf seasonal		Savanna/grass and seasonal woods		Mild/warm grass/shrub	
		μ	Std dev	μ	Std dev	μ	Std dev	μ	Std dev
Channel 1 reflectance (%)	Clear	9.17	3.53	9.79	3.29	10.16	3.20	10.57	3.27
	Smoke	**19.43**	**2.64**	**19.32**	**2.74**	**18.69**	**2.39**	**19.79**	**2.49**
Channel 2 reflectance (%)	Clear	18.87	4.95	19.35	4.57	18.61	4.47	17.48	4.70
	Smoke	**22.98**	**2.23**	**22.57**	**2.60**	**22.04**	**2.43**	**22.89**	**3.31**
Channel 3 temperature (K)	Clear	300.23	3.27	302.12	3.94	304.64	4.92	306.07	6.51
	Smoke	**301.34**	**1.13**	**302.37**	**3.39**	**302.29**	**3.52**	**309.56**	**4.30**
Channel 4 temperature (K)	Clear	292.18	5.46	296.18	5.31	298.02	6.13	299.63	7.63
	Smoke	**292.96**	**1.20**	**297.54**	**2.98**	**297.69**	**3.09**	**302.44**	**3.84**
Channel 4–channel 5 (K)	Clear	3.03	0.73	2.72	0.80	2.71	0.88	2.58	1.10
	Smoke	**1.99**	**0.33**	**2.21**	**0.67**	**2.35**	**0.71**	**2.43**	**1.13**
Channel 3 reflectance (%)	Clear	4.77	2.11	4.31	2.49	4.48	2.81	5.84	3.03
	Smoke	**5.00**	**0.93**	**4.13**	**2.89**	**4.33**	**2.81**	**9.30**	**3.90**
Solar zenith angle (°)	Clear	38.80	4.00	42.43	4.78	43.41	5.34	44.39	6.05
	Smoke	**35.00**	**0.00**	**46.43**	**6.84**	**48.93**	**6.80**	**51.85**	**5.22**
ERBE shortwave flux (W m^{-2})	Clear	160.4	18.41	162.71	13.	159.93	12.58	155.11	14.67
	Smoke	**191.67**	**26.08**	**188.81**	**30.44**	**178.39**	**28.12**	**179.38**	**31.37**
ERBE longwave flux (W m^{-2})	Clear	272.57	10.24	302.63	14.60	306.27	16.09	315.34	16.08
	Smoke	**279.30**	**8.56**	**300.05**	**13.48**	**306.60**	**15.79**	**310.11**	**16.07**
TOVS precipitation (mm day^{-1})		4.29	1.34	2.07	1.18	1.67	0.66	0.96	0.69
TOVS water vapor (cm)		4.37	0.56	3.87	0.58	3.39	0.57	2.89	0.83
TOVS skin temperature (K)		296.30	1.19	299.47	1.85	299.8	2.57	297.37	7.18

lihood estimation technique that employs the measured SW and LW radiances (Wielicki and Green 1989). In this technique, the surface types are identified using standard geographic maps. The surface types include 1) ocean, 2) land, 3) snow, 4) desert, and 5) mixture of land–ocean. Then four basic cloud categories are identified. They are 1) clear (0%–5% cloudy), 2) partly cloudy (5%–50% cloud cover), (3) mostly cloudy (50%–95% cloud cover), and (4) overcast (95%–100% cloud cover). The smoke from biomass burning will be identified into one of the above cloud categories. The uncertainty in scene identification between AVHRR and ERBE was calculated by determining clear-sky pixels from the AVHRR method and comparing this with the ERBE method. Clear-sky pixels identified by the AVHRR method were correctly classified by the ERBE method 76% of the time. The other 24% of the pixels were classified as partly cloudy over land. The ERBE method classified the smoke pixels as partly cloudy most of the time. It is noted that in this comparison, the AVHRR-detected clear and smoky pixels are assumed as truth. Once the pixels are classified into the surface and cloud categories, the ADMs are used to invert the radiances to TOA fluxes. The ADMs (Suttles et al. 1988; Suttles et al. 1989) for the ERBE program were developed using *Nimbus-7* (Taylor and Stowe 1984) and GOES data (Minnis and Harrison 1984a,b,c). Diekmann and Smith (1989) discuss the errors associated with using broadband data for scene identification. Using limited data from April 1985 over two selected oceanic regions, their analysis showed that the ERBE method underestimated cloudiness over the oceans relative to the AVHRR. This resulted in negligible errors in longwave flux, while the errors in shortwave flux reached maximum values of about 13%. The aerosol regions that are classified as partly cloudy could have similar errors in shortwave and longwave fluxes, although it is difficult to precisely estimate their uncertainty. A concerted effort is needed to develop ADMs for aerosols that will reduce uncertainties in direct radiative forcing estimates.

TABLE 5. Mean shortwave, longwave, and net radiative forcing for four ecosystems.

	TRF	TBS	SGW	MGS
SWARF	−40.6	−36.0	−25.3	−35.8
LWARF	6.7	0.7	−0.3	5.3
NETARF	**−33.9**	**−35.3**	**−25.6**	**−30.5**

b. Uncertainties in fire and smoke detection

In this study, a large volume of AVHRR imagery was used to identify fires and smoke. Two different fire detection schemes were discussed. Although the EBAF method appears to perform better than the MKF method, it is tedious and almost impossible to visually ensure that every single fire pixel was accompanied by a smoke plume. The ''accuracy'' of the fire detection scheme was ensured by examining selected AVHRR images for smoke plumes that were associated with fires. False identification of fires was usually associated with coastlines and hot bare surfaces.

In this study, only the smoke around the fire pixels within the ERBE collocated pixel of about 35 km^2 in area is detected. Therefore, the radiative forcing is representative for smoke only around source regions. Our previous study (Christopher et al. 1996) showed that optically thin hazelike smoke has net radiative forcing

values of about -16 W m^{-2}. As noted earlier, the current method may classify low-level warm clouds over the fires as smoke pixels. However, a visual examination of several images showed that directly above fires, smoke is present as opposed to water clouds.

c. *Uncertainties in clear-sky statistics related to radiative forcing*

The AVHRR-based method classifies each AVHRR pixel as clear provided they are not contaminated with clouds or smoke. The narrowband clear-sky statistics presented in Table 4 are consistent with previous studies (Kaufman et al. 1990; Setzer and Perreira 1991). For the collocated analysis, an ERBE pixel was classified as clear only if each AVHRR pixel within the ERBE footprint was classified as clear by the PHC algorithm. However, the clear-sky SW and LW fluxes have a large variability within each ecosystem. For example, the mean clear-sky SW flux for the SGW ecosystem is 155 W m^{-2} with a standard deviation of 15 W m^{-2}, while the mean LW flux is 315 W m^{-2} with a standard deviation of 16 W m^{-2}. Assuming the mean value for computing the radiative forcing terms could therefore lead to uncertainties. We therefore used the minimum and maximum values of clear-sky SW fluxes and recomputed the radiative forcing terms. The net radiative forcing values range from -82 to -14 W m^{-2} for TBS, -70 to -2 W m^{-2} for TBS, -60 to 8 W m^{-2} for SGW, and -68 to 8 W m^{-2} for MGS ecosystems. Due to the large variability of the SW and LW fluxes, the net radiative forcing terms could vary by about 60–70 W m^{-2}; therefore, it is noted that careful attention must be given to ecosystem characterization.

6. Summary

Collocated narrowband and broadband measurements are very useful in evaluating the direct radiative forcing of biomass burning aerosols on a regional scale. In this study, the 1985 biomass burning season between August and October has been studied to monitor fires and smoke and to estimate the direct regional radiative impact of aerosols in four major ecosystems over South America. The AVHRR LAC data are used to detect fires and smoke. The broadband ERBE measurements are used to compute the instantaneous SW, LW, and net radiative forcing of biomass burning aerosols. Two different fire detection schemes are presented. The majority of the fires occur in the SGW and MGS ecosystems, which are broadly called the cerrado regions. The TRF ecosystem (selva) has less than 1% of the total fires that were detected. While the fixed threshold method (MKF) often agrees well with the ecosystem-based threshold method (EBAF), several challenges continue to exist to perform fire detection on a global scale (Kaufman and Justice 1994). Some examples of these challenges include validation and atmospheric correction. The smoke from biomass burning, which often spreads throughout the Amazon basin, has a significant impact on the regional radiative balance. The instantaneous radiative forcing of smoke for the four ecosystems that are studied are negative and range between -25.6 and -33.9 W m^{-2}. A concerted effort has been made to document the narrowband and broadband properties of clear-sky and smoky regions. Both the mean values and standard deviations are provided for all four ecosystems for the 1985 biomass burning season, which could provide useful information for other studies.

Finally, it is noted that biomass burning aerosols play an important role in the regional radiative balance of the earth–atmosphere system. The negative net radiative forcing values for all four ecosystems suggest that the effect is one of cooling. However, in order to extend this regional scale analysis to a global scale, satellite measurements with sufficient temporal sampling should be used, which will permit the estimation of the direct radiative forcing of aerosols on a global scale. The TRMM carries a narrowband radiometer called VIRS that has similar spectral characteristics to that of the AVHRR and will permit the detection of fires and smoke. The TRMM platform also carries a CERES instrument that enables us to estimate the change in TOA fluxes due to aerosol loading. More importantly, the TRMM platform carries both these narrowband and broadband instruments on the same platform in a precessing orbit that will enable tropical regions to be viewed several times during the day. Therefore, to make use of the full capabilities of these two instruments, a viable strategy must be adopted to properly detect aerosols and to estimate their radiative impact.

Acknowledgments. This research was supported by NASA Grant NAGW-3740, managed by Dr. Robert J. Curran, and by NASA New Investigator Program Grant NAGW-5195, managed by Dr. Ghassem Asrar. We would like to thank Ms. Donna Kliche for her help with Fig. 2 and Dr. Kwo-Sen Kuo for the calibration software. One of us (SAC) would also like to thank Dr. Yoram J. Kaufman and Dr. Tim Suttles for their encouragement. We sincerely thank Mr. Rand Feind for a critical reading of this manuscript. The AVHRR data were acquired through the NOAA Satellite Active Archive and the ERBE data were obtained through the Langley DAAC. The TOVS data were acquired through the Goddard DAAC. We thank Ms. Joyce Chou for help with the TOVS data. We sincerely thank Mr. Doug Ross at NOAA and Ms. Sue Sorlie at Langley DAAC for their help with the AVHRR and ERBE data. Appreciation is extended to Connie Crandall for organizing this manuscript.

REFERENCES

Ackerman, S. A., and H. Chung, 1992: Radiative effects of airborne dust on regional energy budgets at the top of the atmosphere. *J. Appl. Meteor.,* **31,** 223–233.

——, and T. Inoue, 1994: Radiation energy budget studies using collocated AVHRR and ERBE observations. *J. Appl. Meteor.*, **33,** 370–377.

Allen, R. C., Jr., P. A. Durkee, and C. H. Walsh, 1990: Snow/cloud discrimination with multispectral satellite measurements. *J. Appl. Meteor.*, **29,** 994–1004.

Anderson, B. E., and Coauthors, 1996: Aerosols from biomass burning over the southern tropical Atlantic region: Distributions and impact. *J. Geophys. Res.*, **101,** 24 117–24 137.

Andreae, M. O., 1991: Biomass burning: Its history, use, and its distribution and its impact on environmental quality and global climate. *Global Biomass Burning*, J. S. Levine, Ed., MIT Press, 1–21.

——, E. V. Browell, M. Garstang, G. L. Gregory, R. C. Hariss, G. F. Hill, and D. J. Jacob, 1988: Biomass burning and associated haze layers over South Amazonia. *J. Geophys. Res.*, **93,** 1509–1527.

Barkstrom, B. R., 1984: The Earth Radiation Budget Experiment (ERBE). *Bull. Amer. Meteor. Soc.*, **65,** 1170–1185.

——, E. Harrison, G. Smith, R. Green, J. Kibler, R. Cess, and the ERBE Science Team, 1989: Earth Radiation Budget Experiment (ERBE) archival and April 1985 results. *Bull. Amer. Meteor. Soc.*, **70,** 154–162.

Baum, B. A., and Coauthors, 1995: Imager clear-sky determination (Subsystem 4.1). *Clouds and the Earth's Radiant Energy System (CERES) Algorithm Theoretical Basis Document, Vol. III, Cloud Analysis and Determination of Improved Top of Atmosphere Fluxes (Subsystem 4)*, CERES Science Team, Eds., NASA, 43–82.

Belward, A. S., P. J. Kennedy, and J.-M. Gregoire, 1994: The limitations and potential of AVHRR GAC data for continental scale fire studies. *Int. J. Remote Sens.*, **15,** 2215–2234.

Cahoon, D. R., B. J. Stocks, J. S. Levine, W. R. Cofer III, and K. P. O'Neill, 1992a: Seasonal distribution of African savanna fires. *Nature*, **359,** 812–815.

——, ——, ——, ——, and C. C. Chung, 1992b: Evaluation of a technique of satellite-derived area estimation of forest fires. *J. Geophys. Res.*, **97,** 3805–3814.

Charlson, R. J., S. E. Schwartz, J. M. Hales, R. D. Cess, J. A. Coakley Jr., J. E. Hansen, and D. J. Hofmann, 1992: Climate forcing by anthropogenic aerosols. *Science*, **255,** 423–430.

Choudhury, B. J., T. J. Dorman, and A. Y. Hsu, 1995: Modeled and observed relations between the AVHRR split window temperatures difference and atmospheric precipitable water over land surfaces. *Remote Sens. Environ.*, **51,** 281–290.

Christopher, S. A., and J. Chou, 1997: The potential of collocated AGLP and ERBE data for fire, smoke and radiative energy budget studies. *Int. J. Remote Sens.*, **18,** 2657–2676.

——, D. V. Kliche, J. Chou, and R. M. Welch, 1996: First estimates of the radiative forcing of aerosols generated from biomass burning using satellite data. *J. Geophys. Res.*, **101,** 21 265–21 273.

Chylek, P., and J. Wong, 1995: Effect of absorbing aerosols on global radiation budget. *Geophys. Res. Lett.*, **22,** 929–931.

Coakley, J. A., R. D. Cess, and F. B. Yurevich, 1983: The effect of tropospheric aerosols on the earth's radiation energy budget: A paramaterization for climate models. *J. Atmos. Sci.*, **40,** 116–138.

Crutzen, P. J., and M. O. Andreae, 1990: Biomass burning in the tropics: Impact of atmospheric chemistry and biogeochemical cycles. *Science*, **250,** 1669–1678.

Diekmann, F. J., and G. L. Smith, 1989: Investigation of scene identification algorithms for radiation budget experiments. *J. Geophys. Res.*, **94,** 3395–3412.

Eidenshink, J. C., and J. L. Faundeen, 1994: The 1 km AVHRR global land data set: First stages of implementation. *Int. J. Remote Sens.*, **15,** 3443–3462.

Fishman., J., 1991: Probing planetary pollution from space. *Environ. Sci. Technol.*, **25,** 612–621.

Flannigan, M. D., and T. H. Vonder Haar, 1986: Forest fire monitoring using NOAA satellite AVHRR. *Can. J. For. Res.*, **16,** 975–982.

Flasse, S. P., and P. Ceccato, 1996: A contextual algorithm for AVHRR fire detection. *Int. J. Remote Sens.*, **17,** 419–424.

Food and Agricultural Organization, 1988: An interim report on the state of forest resources in agricultural countries. Food and Agricultural Organization of the United Nations.

Fraser, R. S., Y. J. Kaufman, and R. L. Mahoney, 1984: Satellite measurements of aerosol mass and transport. *J. Atmos. Environ.*, **18,** 2577–2584.

Frohn, R. C., K. C. McGwire, V. H. Dales, and J. E. Estes, 1996: Using satellite remote sensing analysis to evaluate a socio-economic and ecologic model of deforestation in Rondonia, Brazil. *Int. J. Remote Sens.*, **17,** 3233–3255.

Gentry, A. H., and J. Lopez-Parodi, 1980: Deforestation and increased flooding in the upper Amazon. *Science*, **210,** 1354–1356.

Hao, W. M., and M.-H. Liu, 1994: Spatial and temporal distribution of biomass burning. *Global Biogeochemical Cycles*, **8,** 495–503.

Hartmann, D. L., V. Ramanthan, A. Berroir, and G. E. Hunt, 1986: Earth radiation budget data and climate research. *Rev. Geophys.*, **24,** 439–468.

Hobbs, P. V., J. S. Reid, R. A. Kotchenruther, R. J. Ferek, and R. Weiss, 1997: Direct radiative forcing by smoke from biomass burning. *Science*, **275,** 1776–1778.

Holben, B. N., A. Setzer, T. F. Eck, A. Pereira, and I. Slutsker, 1996: Effect of dry-season biomass burning on Amazon basin aerosol concentrations and optical properties, 1992–1994. *J. Geophys. Res.*, **101,** 19 465–19 481.

Intergovernmental Panel on Climate Change, 1995: *The Science of Climate Change.* Cambridge University Press, 572 pp.

Justice, C. O., and P. Dowty, Eds., 1994: IGBP–DIS satellite fire detection algorithm workshop. Tech. Rep. IGBP–DIS Working Paper 9, 88 pp. [Available from NASA/GSFC, Greenbelt, MD 20771.]

——, J. D. Kendall, P. R. Dowty, and R. J. Scholes, 1996: Satellite remote sensing of fires during the SAFARI campaign using the NOAA Advanced Very High Resolution Radiometer Data. *J. Geophys. Res*, **101,** 23 851–23 863.

Kaufman, Y. J., 1995: Remote sensing of direct and indirect aerosol forcing. *Aerosol Forcing of Climate*, R. J. Charlson and J. Heintzenberg, Eds., J. Wiley and Sons, 298–331.

——, and C. Sendra, 1988: Algorithm for automatic atmospheric corrections to visible and near-IR satellite imagery. *Int. J. Remote Sens.* **9,** 1357–1381.

——, and T. Nakajima, 1993: Effect of Amazon smoke on cloud microphysics and albedo. *J. Appl. Meteor.*, **32,** 729–744.

——, and C. Justice, 1994: The MODIS Algorithm theoretical basis document (version 1.2.2). EOS ID# 2741, NASA/Goddard Space Flight Center, 48 pp.

——, and L. Remer, 1994: Detection of forests using mid-IR reflectance: An application for aerosol studies. *IEEE J. Geosci. Remote Sens.*, **32,** 672–683.

——, and R. S. Fraser, 1997: The effect of smoke particles on clouds and climate forcing. *Science*, **277,** 1636–1639.

——, C. J. Tucker, and I. Fung, 1990: Remote sensing of biomass burning in the tropics. *J. Geophys. Res.*, **95,** 9927–9939.

Kennedy, P., 1992: Biomass burning studies: The use of remote sensing. *Ecol. Bull.*, **42,** 133–148.

Kidder, S. Q., and T. H. Vonder Haar, 1995: *Satellite Meteorology: An Introduction.* Academic Press, 466 pp.

Kidwell, K. B., 1991: NOAA polar orbiter data (*TIROS-N, NOAA-6, NOAA-7, NOAA-8, NOAA-9, NOAA-10, NOAA-11,* and *NOAA-12*) user's guide.

Kingman, S., 1989: Malaria runs riot on Brazil's wild frontier. *New Sci.*, 24–25.

Konzelmann, T., D. R. Cahoon, and C. H. Whitlock, 1996: Impact of biomass burning in equatorial Africa on the downward surface shortwave irradiance: Observations versus calculations. *J. Geophys. Res.*, **101,** 22 833–22 844.

Kopia, L. P., 1986: Earth Radiation Budget Experiment scanner. *Rev. Geophys.*, **24,** 400–406.

Langaas, S., 1992: Temporal and spatial distribution of savanna fires

in Senegal and Gambia, West Africa, 1989–1990, derived from multi-temporal AVHRR night images. *Int. J. Wildland Fire,* **2,** 21–36.

Lanly, J.-P., 1982: Tropical forest resources. Food and Agriculture Organization, United Nations.

Lee, T. F., and P. M. Tag, 1990: Improved detection of hotspots using the AVHRR 3.7-μm channel. *Bull. Amer. Meteor. Soc.,* **71,** 1722–1730.

Malingreau, J. P., G. Stephens, and L. Fellows, 1985: Remote sensing of forest fires: Kalimantan and North Borneo in 1982–1983. *Ambio,* **14,** 314–321.

Matson, M., and G. Stephens, 1987: Fire detection using data from the NOAA-N satellites. *Int. J. Remote Sens.,* **8,** 961–970.

McClain, E. P., 1989: Global sea surface temperatures and cloud clearing for aerosol optical depth estimates. *Int. J. Remote Sens.,* **10,** 763–769.

McDougal, D., 1995: Smoke, Clouds and Radiation-Brazil (SCAR-B) Field Experiment, August 16 to September 14, 1995. Mission plan prepared by SCAR-B scientists and the SCAR-B Project Office. NASA Special Publication, NASA/Langley Research Center, Hampton, VA, 164 pp.

Meillo, J. M., C. A. Palm, R. A. Houghton, G. M. Wodell, and N. Myers, 1985: A comparison of recent estimates of disturbance in tropical forest. *Environ. Conservation,* **12,** 27–40.

Minnis, P., and E. F. Harrison, 1984a: Diurnal variability of regional cloud and clear-sky radiative parameters derived from GOES data. Part I: Analysis method. *J. Climate Appl. Meteor.,* **23,** 993–1011.

——, and ——, 1984b: Diurnal variability of regional cloud and clear-sky radiative parameters derived from GOES data. Part II: November 1978 cloud distributions. *J. Climate Appl. Meteor.,* **23,** 1012–1031.

——, and ——, 1984c: Diurnal variability of regional cloud and clear-sky radiative parameters derived from GOES data. Part III: November 1978 radiative parameters. *J. Climate Appl. Meteor.,* **23,** 1032–1051.

——, ——, L. L. Stowe, G. G. Gibson, F. M. Denn, D. R. Doelling, and W. L. Smith Jr., 1993: Radiative climate forcing by the Mount Pinatubo eruption. *Science,* **259,** 1411–1415.

Molofsky, J., C. A. S. Hall, and N. Myers, 1986: Comparison of tropical forest surveys. U.S. Department of Energy.

Myers, N., 1991: Tropical forests: Present status and future outlooks. *Climate Change,* **19,** 3–32.

Nobre, C. A., P. S. Sellers, and J. Shukla, 1991: Amazon deforestation and regional climate change. *J. Climate,* **4,** 957–988.

Olson, J. S., 1991: World ecosystems (WE1.3 and WE1.4) digital raster data on global geographic (LAT/lon) 180X360 and 1080X2160 grids. NOAA National Geophysical Data Center, Boulder, CO.

Penner, J. E., R. E. Dickinson, and C. A. O'Neill, 1992: Effects of aerosol from biomass burning on the global radiation budget. *Science,* **256,** 1432–1434.

——, and Coauthors, 1994: Quantifying and minimizing uncertainty of climate forcing of anthropogenic aerosols. *Bull. Amer. Meteor. Soc.,* **75,** 375–400.

Price, J. C., 1984: Land surface temperature measurements from the split-window channels of the *NOAA-7* Advanced Very High Resolution Radiometer. *J. Geophys. Res.,* **89,** 7231–7237.

Prins, E. M., 1994: Trends in South America biomass burning detected with the GOES VAS from 1983–1991. *J. Geophys. Res.,* **99,** 16 719–16 735.

——, and W. P. Menzel, 1992: Geostationary satellite detection of biomass burning in South America. *Int. J. Remote Sens.,* **13,** 2783–2799.

Ramanathan, V., R. D. Cess, E. F. Harrison, P. Minnis, B. R. Barkstrom, E. Ahmad, and D. Hartmann, 1989: Cloud radiative forcing and climate: Results from the Earth Radiation Budget Experiment. *Science,* **243,** 57–63.

Rao, C. R. N., Ed., 1993a: Degradation of the visible and near-infrared channels of the Advanced Very High Resolution Radiometer on the *NOAA-9* spacecraft: Assessment and recommendations for corrections. NOAA Tech. Rep. NESDIS 70, 21 pp. [Available from National Oceanic and Atmospheric Administration, Washington, DC 20233.]

——, J. T. Sullivan, C. C. Walton, J. W. Brown, and R. H. Evans, 1993b: Nonlinearity corrections for the thermal infrared channels of the Advanced Very High Resolution Radiometer. Assessment and recommendations. NOAA Tech. Rep. NESDIS 69, 31 pp. [Available from National Oceanic and Atmospheric Administration, Washington, DC 20233.]

Reichle, H. G., Jr., and Coauthors, 1986: Middle and upper tropospheric carbon monoxide mixing ratios as measured by a satellite-borne remote sensor during November 1981. *J. Geophys. Res.,* **91,** 10 865–10 887.

Robinson, J. M., 1991: Fire from space: Global fire evaluation using infrared remote sensing. *Int. J. Remote Sens.,* **12,** 3–24.

Schwartz, S. E., 1988: Are global albedo and climate controlled by marine phytoplankton? *Nature,* **336,** 441–445.

Seiler, W., and P. J. Crutzen, 1980: Estimates of gross and net fluxes of carbon between the biosphere and atmosphere from biomass burning. *Climate Change,* **2,** 207–247.

Setzer, A. W., and M. C. Perreira, 1991: Amazonia biomass burnings in 1987: An estimate of their tropospheric emissions. *Ambio,* **20,** 19–22.

Susskind, J., J. Rosefield, D. Reuter, and M. T. Chahine, 1984: Remote sensing of weather and climate parameters from HIRS2/MSU on TIROS–N. *J. Geophys. Res.,* **89,** 4677–4697.

Suttles, J. T., and Coauthors, 1988: Angular radiation models for earth–atmosphere system. Shortwave radiation, Vol. I, NASA Ref. Publ. 1184, 147 pp.

——, R. N. Green, G. L. Smith, B. A. Wielicki, I. J. Walker, V. R. Taylor, and L. L. Stowe, 1989: Angular radiation models for earth–atmosphere system. Longwave radiation, Vol. II, NASA Ref. Publ. 1184, 84 pp.

Tanre, D., P. Y. Deschamps, C. Devaux, and M. Herman, 1988: Estimation of Saharan aerosol optical thickness from blurring effects in Thematic mapper data. *J. Geophys. Res.,* **93,** 15 955–15 964.

Taylor, V. R., and L. L. Stowe, 1984: Reflectance characteristics of uniform earth and cloud surfaces derived from *NIMBUS-7* ERB. *J. Geophys. Res.,* **89,** 4987–4996.

Townshend, J. R. G., C. O. Justice, and V. Kalb, 1987: Characterization and classification of South American land cover types using satellite data. *Int. J. Remote Sens.,* **8,** 1189–1207.

Tucker, C. J., N. N. Holben, and T. E. Goff, 1984: Intensive forest clearing in Rondonia, Brazil, as detected by satellite remote sensing. *Remote Sens. Environ.,* **15,** 255–261.

Uhl, C., R. Buschbacher, and E. A. S. Serrao, 1988: Abandoned pastures in eastern Amazonia, I: Patterns of plant succession. *J. Ecol.,* **76,** 663–681.

Ward, D. E., and Coauthors, 1992: Smoke and fire characteristics for cerrado and deforestation burns in Brazil: BASE-B experiment. *J. Geophys. Res.,* **97,** 14 601–14 619.

Weaver, J. F., J. F. W. Purdom, and T. L. Schneider, 1995: Observing forest fires with the *GOES-8* 3.9-μm channel. *Wea. Forecasting,* **10,** 803–808.

Wielicki, B. A., and R. N. Green, 1989: Cloud identification for ERBE radiative flux retrieval. *J. Appl. Meteor.,* **28,** 1133–1146.